

MULTIGRID COMPUTATION OF TRANSONIC FLOW ABOUT COMPLEX AIRCRAFT CONFIGURATIONS, USING CARTESIAN GRIDS AND LOCAL REFINEMENT.

B.Epstein, A.L.Luntz and A.Nachshon

Israel Aircraft Industries, Ben Gurion Airport, Israel.

Abstract.

A three dimensional full potential code is described, able to handle arbitrary aircraft configurations. This code is based on the use of cartesian grids, local refinement and multigrid calculations. The configuration is treated as an assembly of elements (bodies, wings, pylons etc.). The algorithm incorporates the solution of the complicated problem of body boundary condition implementation, for nonaligned grids. Some other new problems, such as the multigrid treatment of local refinements and grid overlapping, had to be resolved during the code design. Three application cases are described: 1) A fighter configuration, including body, wing, fairing and canard; this example shows the importance of the grid-to-shock alignment, which is possible with the flexible choice of local grids (and sometimes impossible in codes with fixed mesh grids). 2) A fighter configuration, including body, wing, fairing, canard and external fuel tank; the analysis shows an unexpectedly strong interference between body, wing and the fuel tank. 3) A civil aircraft configuration, with different wing root fairings; this case shows the role of the fairing on the wing pressure distribution.

1. Introduction.

In the recent years, the need for computational transonic aerodynamic codes able to handle arbitrary configurations has been widely recognized. It is also recognized that it is unrealistic to design one universal method able to generate a mesh grid about any given configuration, just by mapping the outside of the configuration onto a semispace.

Three main ways have been used to overcome these difficulties (for various approximations to the complete flow equations, including potential and Euler). One of the methods creates smooth local mesh grids, aligned to the body surface, and then tailors them into one universal grid (e.g., /1/ in the framework of finite elements, /2/ with finite differences and finite volumes). This approach is virtually unlimited in handling complicated configurations, but is far from being fully automated (it demands usually months, for an experienced engineer, to complete a grid about a new complicated configuration).

Another way is recently explored (/3/, /4/), using unstructured (but still body aligned) grids, automatically generated from a cloud of vertices. This cloud originates from a collection of separate grids, each one - about a different element of the configuration. There are still some difficulties to overcome in order to make this very promising (and fully automatic) approach really universal for 3 dimensional configurations. It also has all the drawbacks of fully nonregular grids.

The third way is the use of cartesian grids. They provide a simple and good approximation to the governing equations in the free air. They are not

body surface aligned and thus eliminate almost all the problems of grid generation. At the same time, the use of cartesian grids introduces several other serious problems, first of all the body boundary condition implementation. Several efforts have been made to use cartesian grids (e.g., /5/, /6/, /7/). In all these works, their authors see the ability of handling arbitrary 3-D configurations as their main goal. We believe that the failure to achieve this goal is due to the fact that not all the problems arising from the use of cartesian grids have been solved in these works.

The present paper describes a 3 dimensional full potential code which uses uniform cartesian (not necessarily rectangular) grids. We use local grid refinement, to achieve the needed resolution without overloading the computer memory with grid points. We use the multigrid approach, not only to speed up the computation but mainly to hold all the local grids together in the field solution. We have found a solution to the difficult problem of body boundary condition implementation in nonaligned grids, as may be seen from the results. We handle a given aircraft configuration as a Boolean sum of bodies.

The basic features of the code have been described in previous publications (/8/, /9/). However, we start this paper with a description of the algorithm, for completeness and also to provide some details not previously described.

The main purpose of this paper is to show the abilities of the code in solving problems of analysis and design of practical configurations. As the code solves full potential flows, we have chosen examples where the flow is mainly potential. At the present time, a 3-D Euler code, based on similar principles, is completed and under evaluation, to be described in a future publication.

Three application cases are described in the present paper:

- A fighter configuration, including body, wing, fairing and canard. This example shows the importance of the grid-to-shock surface alignment, which is possible with the flexible choice of local grids (and sometimes impossible in codes with fixed mesh grids).

- A fighter configuration, including body, wing, fairing, canard and external fuel tank. The analysis shows an unexpectedly strong interference between body, wing and the fuel tank.

- A civil aircraft configuration, with different wing root fairings. This case shows the role of the fairing on the wing pressure distribution.

2. Equation and Numerical Scheme.

The equation solved is the "nonconservative" full potential equation

$$LF \equiv (a^2-u^2)F_{xx} + (a^2-v^2)F_{yy} + (a^2-w^2)F_{zz} - 2uvF_{xy} - 2uwF_{xz} - 2vwF_{yz} = 0 \tag{1}$$

where $F(x,y,z)$ is the full potential, $u=F_x$, $v=F_y$, $w=F_z$ are the velocity components and a is the local sound speed,

$$a^2 = 1/M^2 + (\gamma - 1) \cdot (1 - u^2 - v^2 - w^2) / 2,$$

M being the free stream Mach number.

In the actual computation, the reduced potential

$$\varphi = F - x \cos \alpha - y \sin \alpha$$

is used, where α is the angle of attack.

Thus, the problem solved is inviscid. The boundary layer, if needed, has to be added to the aircraft shape prior to the potential calculation.

The wakes of the lifting surfaces are assumed to be composed of straight lines parallel to the x -axis starting from the trailing edge of the lifting surface.

The boundary conditions at infinity are $\varphi = 0$ everywhere except the downwind ($x = +\infty$) infinity, where $\partial \varphi / \partial x = 0$ is imposed.

Boundary condition at the aircraft surface is the homogeneous Neumann $\partial F / \partial n = 0$, n - normal to the surface.

Besides rectangular grids, grids with sweep and dihedral are used.

Equation (1) is discretized using symmetrical schemes for derivatives at points that appear subsonic ($u^2 + v^2 + w^2 < a^2$) in the last iteration made, and streamwise upwind schemes at supersonic points. The system of finite difference equations is iterated by SLOR in x - or/and y -directions, with the Seidel-type sweep.

3. Discretized Boundary Conditions.

With nonaligned grids, the implementation of the body boundary condition becomes a complicated problem, and its successful solution is a major condition for the success of the method as a whole.

Thorough analysis shows that the finite volume approach with nonaligned grids (/6/, /7/), which is very attractive in some well defined cases, becomes extremely complicated when the algorithm is supposed to deal with arbitrary configurations. For this reason, the finite difference approach was chosen.

The implementation of the body boundary condition consists of assigning, before and after every iteration on a given grid, the potential value for every dummy point participating in a templet of any field grid point. The potential value $F(D)$ at the dummy point D has to express, as related to the field potential values $\{F\}$, the Neumann boundary condition. $F(D)$ depends on the field potential values as well as on the position of the real (field) point R , to whose templet D belongs (fig.1) :

$$F(D) = B(D, R, \{F\}). \quad (2)$$

The B formula is constructed in several steps.

a) Point D is reflected (fig.1), from inside the body, into the point RD , across the tangent plane to the body surface, as advised in /12/. $F(D)$ will be defined equal to the interpolated $F(RD)$, thus avoiding unnecessary extrapolations.

b) Not every interpolation into RD may be accepted. Indeed, if D is very near to the surface (like D^* , fig.1), then the interpolation to RD is almost interpolation to D itself and thus does not incorporate the Neumann condition. For this reason, the interpolation to RD uses itself a formula, bearing the Neumann condition: $ct^2 + d$, where t is the coordinate along the normal n to the body surface, with $t=0$ at the tangent plane. Coefficients c and d are

selected with the least square method. The least square uses projections, on the normal n , of field grid points, chosen from the nearest to RD , but also dispersed enough on the normal (compared with the mesh size).

c) The values at the projected points are the potential values at the points before projection, corrected by the stream velocity vector near RD .

As to the boundary conditions at the local refinement box limits, they are fixed, during the iteration process for every specific local grid, as Dirichlet conditions, and are corrected each time by the coarse-to-fine correction interpolation in the multigrid process. The exception is for the symmetry plane (if defined), where the reflection condition is used. At the front (upwind) side of any local refinement box, potential values at an additional grid plane are defined during the coarse-to-fine grid interpolation. These values are used in the upwind schemes, only if and where the local stream velocity appears to be supersonic.

4. Preprocessor and Computational Code.

The code consists of two main programs: PREPRO and MULTIG. The purpose of PREPRO is to translate the geometry of a given configuration in terms of computational grids. It works independently for each grid. The access to the geometry data is made through a number of subroutines, which answer the following questions:

- is a given point inside the aircraft or in the air?
- for two points A and B , A being outside the aircraft, is B seen from A ? If not, what is the last point C , on the A - B interval, seen from A , and what is the normal to the surface, at C ?
- location of trailing edge of a lifting surface.

The configuration is treated as an assembly (Boolean sum) of elements. At present, the following elements are allowed: bodies (fuselage, external fuel tank, bomb etc.), wings (also canards, horizontal tail etc.), pylons (also fins), nacelles. Several elements of one type may be present in one configuration. Only in these subroutines there are constraints on the configuration.

The PREPRO output, together with the multigrid data (grids, multigrid steps) and parameters (Mach, angle of attack, relaxation parameters etc.), are the input to MULTIG. In the multigrid calculation process, fine-to-coarse corrections ("right hand side", RHS) are used explicitly for all operators involved, except for the operator B , which defines the dummy point potential values (in our case, it seems to be too complicated technically, to introduce RHS for B). This exception, of course, slows down the convergence rate.

5. Multigrid Level Interaction and Local Refinement.

If fine grid h is a local refinement of a coarse grid H , both the coarse-to-fine and the fine-to-coarse corrections (e.g., /10/) create problems for points, inside the fine grid box G^h , near its limits. One of the problems is the fine-to-coarse operator correction RHS to the coarse grid operator:

$$L^H F^H = RHS^H, \quad (3)$$

where RHS^H is defined usually as

$$RHS^H = L^H (I_H^H F^h) - I_H^H (L^h F^h - RHS^h) \quad (4)$$

I_h^H being the fine-to-coarse interpolation operator. For a coarse grid point R, which itself belongs to the fine grid box G^h (so that I_h^H appoints for it a potential value), $L^H(I_h^H F^h)$ may be undefined, because some of the points in the templet of R may be outside G^h . Even if all of the templet points are inside G^h , but some of them are dummy, the formulae (2) for their potential value calculation (as coarse grid points) may include points outside G^h , so that RHS^H is still not defined by (4), (2).

At such points R, it is usually advised (/11/, p.93) to neglect the RHS^H . Our experience shows that this advice is acceptable only when the local refinement ends with the solution becoming smooth, i.e. where RHS^H is small. Our case is different. We use local refinement wherever we need better resolution; we may end refinement where it is not needed, although the solution may still be not smooth (and the RHS^H large). If so, the RHS^H has to be calculated everywhere in G^h , otherwise the solution process becomes unstable.

To define RHS^H everywhere in G^h , we use extrapolated field values

$$F_{new}^H = F_{old}^H + E_H (I_h^H F_{new}^h - F_{old}^H)$$

instead of $I_h^H F_{new}^h$, for real points, where E^H is an extrapolation operator, and

$$F_{new}^H(D) = B^H(D, F_{old}^H) + SB^H(D, F_{new}^h - F_{old}^H)$$

for dummy, where B^H is the regular boundary condition operator in the coarse grid, (2), and SB^H is shortened boundary condition operator, using as arguments potential values at the coarse grid real points inside G^h only. The operator which appoints to D the potential value at its reference point (see above, the B definition), may be used as SB^H .

6. Multigrid Treatment of the Potential Wake Jump.

The potential jump W across the wake of a lifting surface is a local value as a function of the span station, but it is an integral value for a fixed span station, insofar as it remains constant along the x-coordinate line. For this reason, W needs multigrid treatment somehow different from that of other functions involved (potential, boundary conditions at infinity, boundary conditions at the symmetry plane and the grid box sides), whose values are purely local.

For a given span station, in a given mesh grid, we define the calculated potential jump CW as the difference of potential values extrapolated to the wing surface, from grid points above and below the wing, near the trailing edge. For stations outside the wing span, $CW = 0$.

For a function $g(k)$ of span station k, defined not for every k of a given grid (but at least for one of them), the operator $IW(g)$ extends the definition of g to all the span stations, with homogeneous Neumann conditions at the box limits (if needed).

Coarse-to-fine W interpolation:

$$W^h = W_{old}^h + I_H^h (W^H - I_H^h W_{old}^h) \cdot RL1,$$

where W_{old}^h is the W value after the last calculation in the h grid, RL1 - relaxation parameter (usually between .5 and 1).

Fine-to-coarse correction:

$$RHSW^H = IW(I_h^H W^h - CW^H) + I_h^H (RESW^h),$$

where

$$RESW^h = IW(RHSW^h - W_{last}^h + CW^h),$$

at the finest level $RHSW^h = 0$.

Vortex relaxation (with the iteration process):

$$W_{n+1}^H = W_n^H + IW(RHSW^H - W_n^H + CW^H) \cdot RL2$$

7. Overlapping.

With local refinement, several grids may be used at the same multigrid level. This may occur for different reasons, such as limited core memory and, as a result, the need to divide one large grid into several smaller ones, or the use of different types of grids at the same refinement level (for example, a rectangular grid covering a part of the fuselage and the fairing, and a swept grid along the wing leading edge).

Some of these grids may overlap. In such a case, computational instability may occur, if the coarse grid G^H receives, at some point R, the RHS^H from one of the overlapping fine grids G_1^h, G_2^h and, after a relaxation with this RHS^H , sends the coarse-to-fine correction to the second overlapping grid.

To avoid this conflicting situation, restriction on the use of overlapping is introduced. For any two grids G_1^h and G_2^h covered by one coarser level grid G^H , overlapping is only allowed, such that every grid point of G^H is strictly inside not more than of one of the fine grids G_1^h, G_2^h .

For the exchange of information between overlapping grids, grid limit points of one of the overlapping grids, say G_1^h , falling inside G_2^h , are given, after each iteration, potential values interpolated from G_2^h , and vice versa.

8. The Grid-to-Shock Alignment.

This application case deals with a wing-body-fairing-canard fighter configuration. Computations were made for $M = .9$, $\alpha = 6^\circ$ (which corresponds to approx. $C_L = .32$). For these flight conditions, the experiment shows no signs of developed separation, thus we may expect good agreement between experiment and full potential calculation.

However, the computation using 5 grid levels with swept grids (fig.2) on the finest (5th) level, shows a completely smeared shock (fig.3). Similar results are given by Jameson's FLO22 wing-only full potential code (fig.3 shows the comparison at the $\eta = .67$ span station, outboard to the canard).

From the experiment, one may learn that the shock line, at the wing upper surface, is nearly parallel to the wing trailing edge (fig.4), thus making a large angle with the spanwise grid lines of the finest multigrid level. The same applies to the FLO22 grid lines. In both cases, the templet of any grid point near the shock uses points lying far ahead and behind the shock (fig.5), which leads to the shock smearing in computation.

With rectangular grids (fig.6), used at the 5th level instead of swept grids, the corresponding templet points (fig.7) are much nearer to the shock. This may be the reason for a completely different, good agreement with the experiment (fig.8).

Flexible choice of local grids gives the possibility of an approximate grid-to-shock alignment for every configuration. It should be emphasised that no full grid-to-shock alignment is needed for a satisfactory shock representation. Sometimes preliminary calculations may help to find appropriate local grids.

9. Fighter Configuration with External Fuel Tank.

This configuration includes fuselage, wing, canard and a large external fuel tank (fig.9). The geometry used in the computation is an exact description of the wind tunnel model, except for the exclusion of the fuel tank pylon.

The computation used 6 grid levels, with the grids of the finest (6th) level around the fuel tank and the part of the wing above it (fig.10). The computation was done at the cruise flight conditions $M = .9$, $\alpha = 2^\circ$.

As could be expected, the shock originated by the irregularity of the fuel tank shape, is amplified by the wing-tank close coupling (fig.11) and appears both on the fuel tank upper surface and on the neighbouring wing lower surface (fig.12,13). Less expected was the effect of the fuselage-fuel tank coupling in extending the shock from the tank to the fuselage (fig.14).

To reduce the wave drag of the configuration, the prime source of the shock - the unsatisfactory curvature of the fuel tank surface - was treated (fig.15). With the modified fuel tank shape, the calculated C_D of the configuration was reduced by 24 counts. The major part of this reduction is due to the weakening of the wing-tank-fuselage interaction induced shock (fig.16-18). On the isolated fuel tank, the modification reduced the drag by 4 counts only.

The experiment confirmed the computational prediction: with $\alpha = 2^\circ$ and Mach number between .9 and .95, the drag reduction is between 20 and 25 counts.

10. Civil Aircraft, Wing-Body Fairing.

The civil aircraft configuration includes fuselage, low-mounted wing and fairing. A wind tunnel experiment has been made with the model, at $Re = 3.5$ million.

Boundary layer was added to the wing-fairing geometry, prior to the computations. Computations used 7 grid levels at the body, fairing and inboard wing (fig.20), 8 levels at the outboard wing. Comparison shows good agreement between computation and experiment (fig.21).

Pressure distribution at the inboard sections (including fairing) shows a double shock, both in computation and experiment. It is due to several features of the geometry:

a) The root profile upper surface is too flat, between 20% and 50% of the chord. This leads to a lower stream velocity in that region and creates a "valley" in the C_D distribution (fig.22).

b) The curvature at the upper surface rear part of the root profile is too high, thus overaccelerating the flow.

c) Another source of the flow overacceleration, in this region, is the curvature of the fairing, on the side of the body (fig.23).

d) The third source of the flow acceleration, at the root trailing edge, is the low position of the wing and the crossflow, from the wing to the underneath of the body.

Modification of the fairing was made, to eliminate or diminish these undesirable features of the geometry. To increase the resolution of the airflow computations supporting this redesign, a new grid was added at the fine, 7th grid level, in the fairing - trailing edge region (fig.20). Calculations were made at $M = .8$, $\alpha = 1.5^\circ$ (both C_L and M slightly higher than cruise conditions).

The new fairing (fig.24-27) consists of two elements. The first is a local "wall", eliminating c) and decreasing d) (fig.24,25,26). The second element is an addition to the inboard wing section, to correct a) and b) (fig.27).

Fig.28 shows the new C_D distribution at several inboard sections, as compared to the previous distributions. The C_D distributions improved considerably even beyond the crank ($\eta = .37$), far outside the fairing (which ends at $\eta = .17$).

The resulting computed decrease in C_D is 17 counts.

Acknowledgements.

Prof. A. Brandt's consultations in the Multigrid have been very useful in the algorithm design. I. Darel supported the project in the IAI and helped to clarify many engineering problems in the applications. B. Bilu and Dr. S. Yaniv took part in the computational work. We are deeply grateful to them all.

References.

1. Bristeau, M.O., Pironneau, O., Glowinski, R., Periaux, J., Perrier, P. and Poirier, G. "On the Numerical Solution of Nonlinear Problems in Fluid Dynamics by Least Squares and Finite Element Methods (II). Applications to Transonic Flow Simulations". Proc. 3rd International Conference on Finite Elements in Nonlinear Mechanics, FENOMECH 84, Stuttgart, 1984, edited by J. St. Doltsinis, North Holland, 1985, pp.363-394.
2. Fritz, W., "Numerical Grid Generation around Complete Aircraft Configurations". AGARD 58th Meeting on Applications of Computational Fluid Dynamics in Aeronautics, 7-10 Apr. 1986, Aix-en-Provence, France.
3. Jameson, A., Baker, T.J. and Weatherill, N.P., "Calculation of Inviscid Transonic Flow over a Complete Aircraft", AIAA Paper 86-0103, AIAA 24th Aerospace Sciences Meeting, Reno, Jan. 1986.
4. Jameson, A. and Baker, T.J. "Improvements to the Aircraft Euler Method". AIAA Paper 87-0452, AIAA 25th Aerospace Sciences Meeting, Reno, 1987.
5. Reyhner, T.A., "Three-Dimensional Transonic Potential Flow about Complex Three-Dim. Configurations". NASA Report 3814, 1984.
6. Wedan, B. and South, J.C., "A Method for Solving the Transonic Full Potential Equation for General Configurations". AIAA Paper 83-1889, 1983.
7. Gaffney, R.L., Hassan, H.A. and Salas, M.D., "Euler Calculations for Wings using Cartesian Grids." AIAA Paper 87-0356, AIAA 25th Aerospace Sciences Meeting, Reno, 1987.
8. Luntz, A.L. and Epstein, B., "A Multigrid Full Potential Transonic Code for Arbitrary Configurations". GMD-Studien Nr.110, Proceedings of the 2nd European Conference on Multigrid Methods, Koeln, 1985.

9. Luntz, A.L. and Epstein, B., "Full Potential Transonic Code for Arbitrary Configurations" Collection of Papers of the 28th Israel Annual Conference on Aviation and Astronautics, 1986.

10. Brandt, A. "Multi-Level Adaptive Computations in Fluid Dynamics". AIAA J. 18(1980), pp. 100-108.

11. Brandt, A. "Multigrid Techniques: 1984 Guide". The Weizman Institute of Science, Rehovot, Israel, 1984.

12. Abarbanel, S., "Supersonic Flow About Blunt-Nosed Bodies, at Angle of Attack." Report, Tel-Aviv University, 1977.

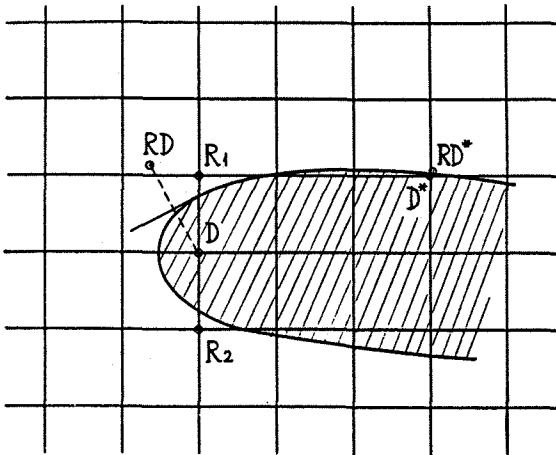


Fig. 1. Potential values at D as dummy in templets of points R_1 and R_2 may be different

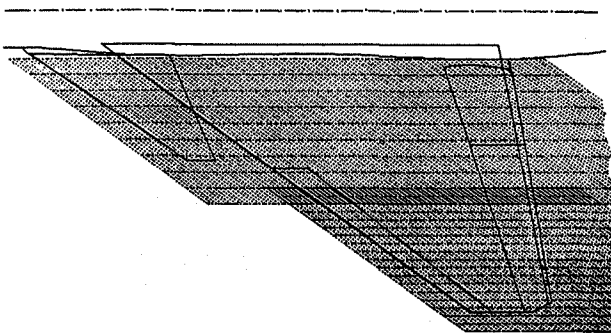


Fig. 2. Fighter configuration with swept grids of the fine grid level. Planform.

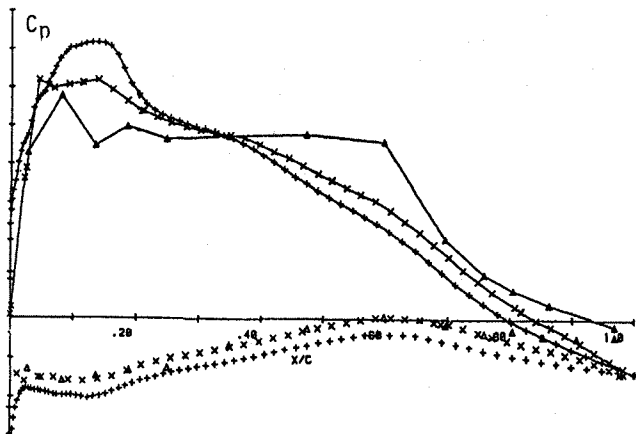


Fig. 3. C_p distribution, wing section, $\eta = .67$.
 -▲-▲-▲- experiment
 ++++++ FLO22 computation
 xxxxxxxx present method, swept grids

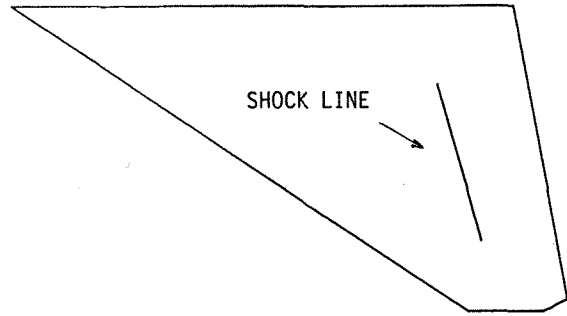


Fig. 4. Fighter wing, shock position.

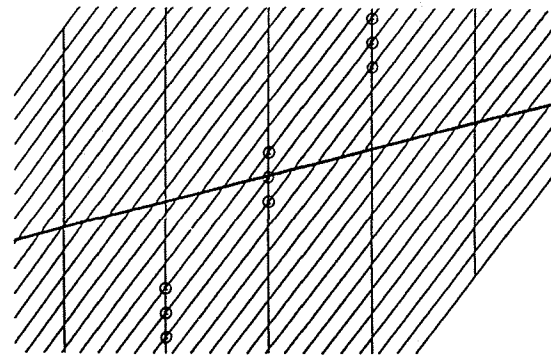


Fig. 5. Swept grid, templet, shock position.

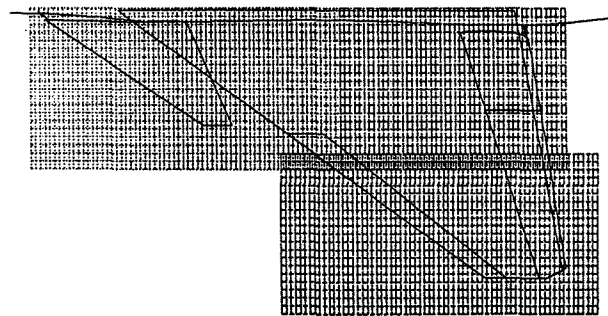


Fig. 6. Fighter configuration with rectangular grids at the fine level. Planform.

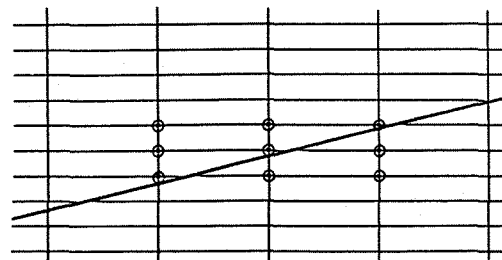


Fig. 7. Rectangular grid, templet, shock position.

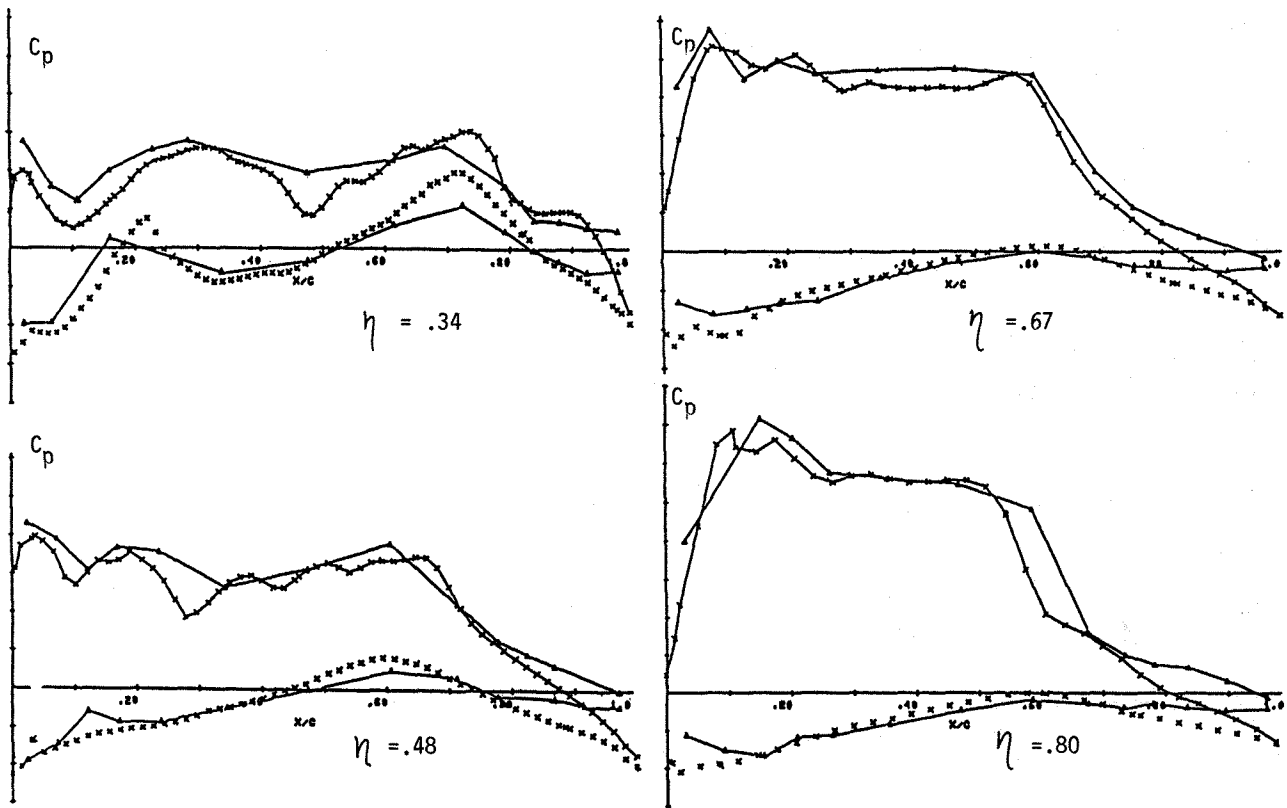


Fig.8. Fighter configuration, wing-body-fairing-canard. C_p distribution, $M=.9$, $\alpha=6^\circ$.
 experiment
 present method, rectangular fine grids
 (approx. shock aligned).

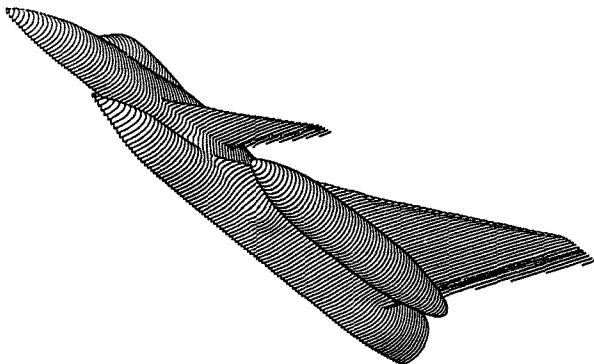


Fig.9. Fighter configuration, wing - body - fairing - canard - external fuel tank.

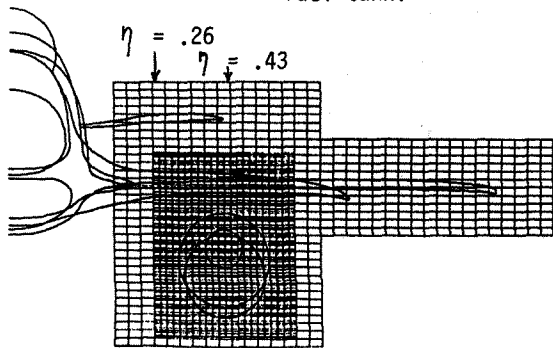


Fig.10. Fighter configuration, with grids of the finest levels, cuts normal to the body axis.

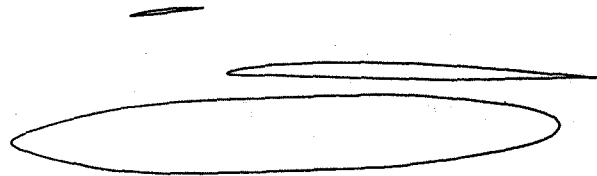


Fig.11. Fighter configuration, vertical cut along the fuel tank axis.

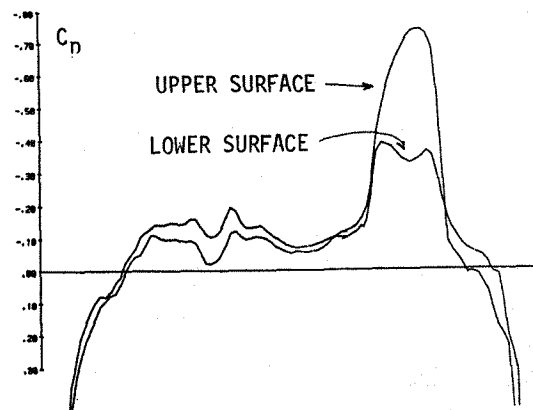


Fig.12. C_p distribution along the fuel tank center line plane, upper and lower surfaces of the fuel tank. $M = .9$, $\alpha = 2^\circ$.

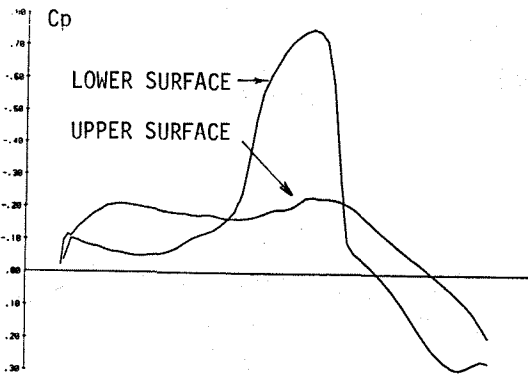


Fig. 13. C_p distribution along the fuel tank center line, wing upper and lower surface, $\eta = .43$.

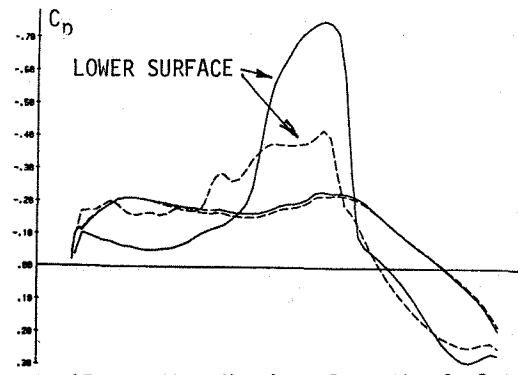


Fig. 17. C_p distribution along the fuel tank center line, wing upper and lower surface, $\eta = .43$. — with old fuel tank, ---- with new fuel tank.

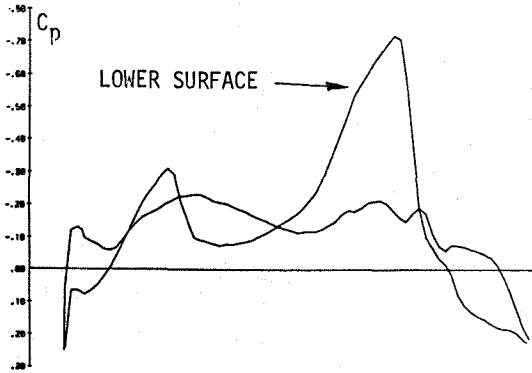


Fig. 14. C_p distribution at the wing section, $\eta = .23$, between fuel tank and body.

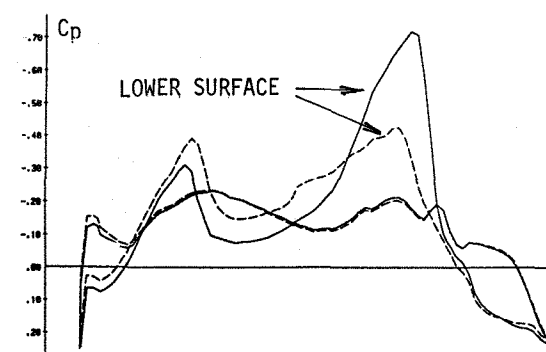
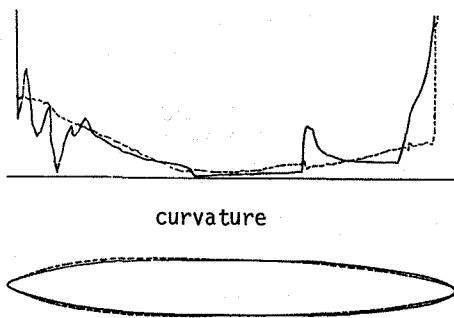


Fig. 18. C_p distribution, wing, $\eta = .26$, between body and fuel tank. — with old fuel tank, ---- with new tank.



Fuel tank, old and new.

Fig. 15. Fuel tank center line cut, and its curvature.

— old shape
---- new shape

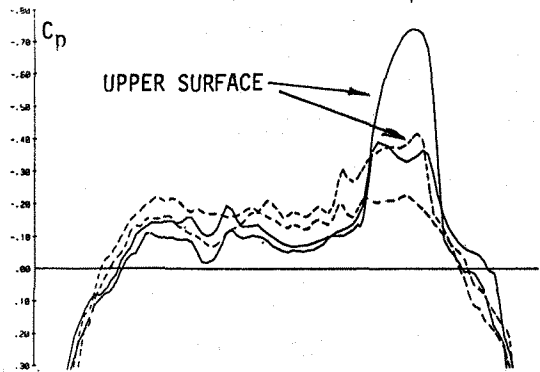


Fig. 16. C_p distribution along the fuel tank center line. — old, ---- new.

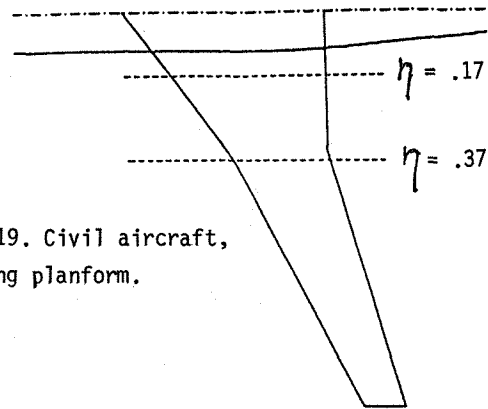


Fig. 19. Civil aircraft, wing planform.

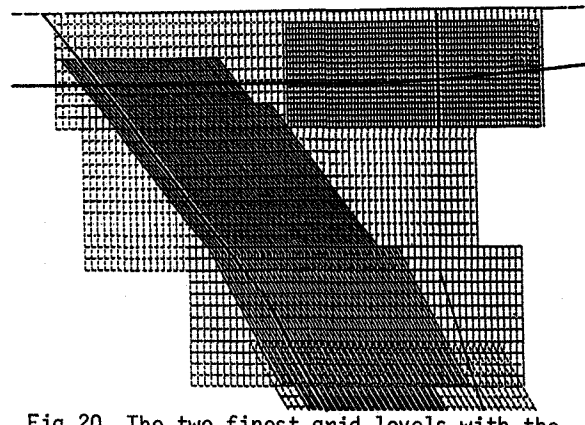


Fig. 20. The two finest grid levels with the civil aircraft planform, inboard.

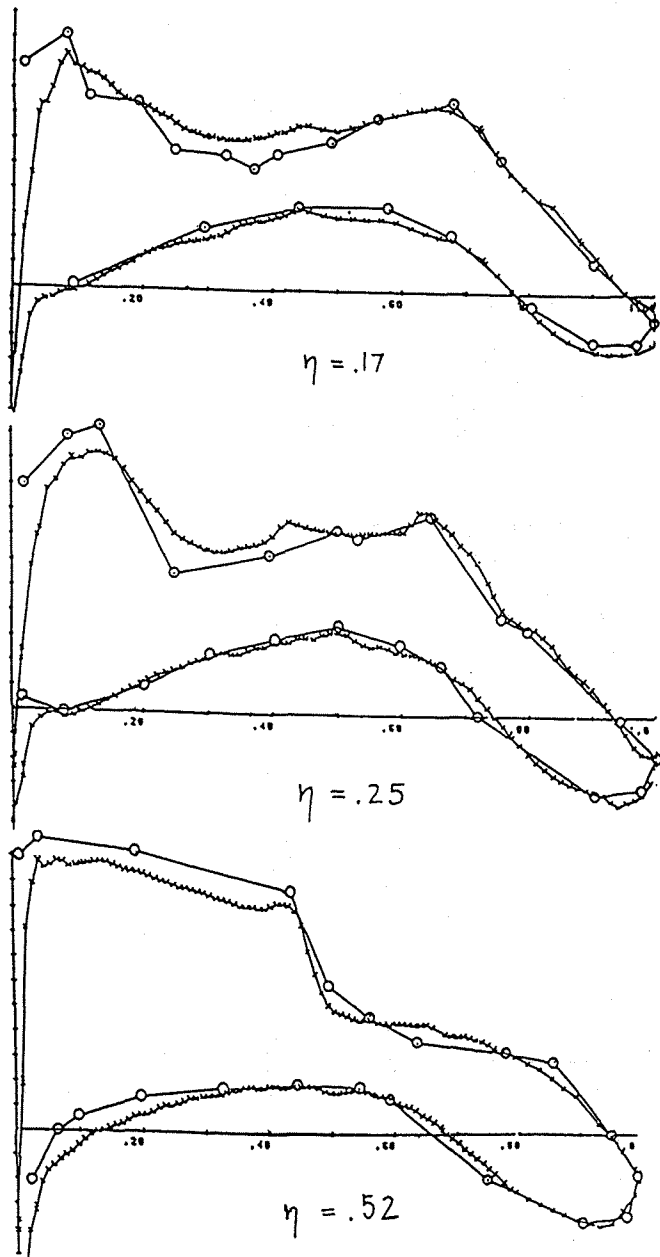


Fig.21. Civil aircraft, C_p distribution at several inboard sections of the wing, with the original fairing. $M = .8$, $\alpha = 2^\circ$.
 —○— experiment, —x— present method

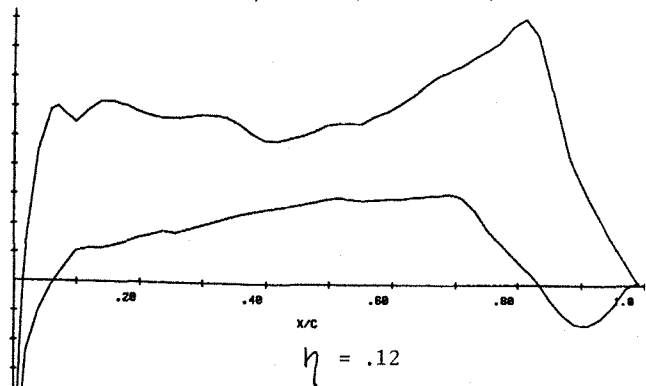


Fig.22. C_p distribution at the wing - fairing root section. $M = .8$, $\alpha = 1.5^\circ$.

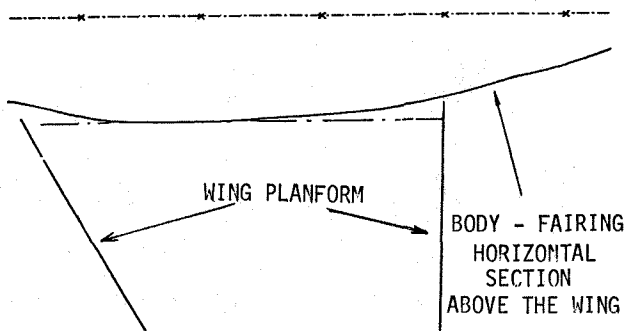


Fig.23. Civil aircraft, horizontal cut of the body - fairing, just above the wing.

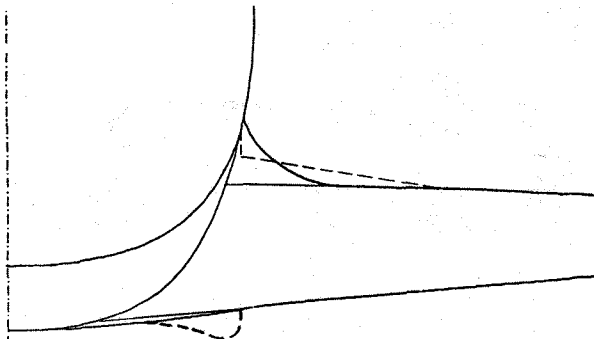


Fig.24. Civil aircraft, cross-section normal to the body axis. ---- new fairing.

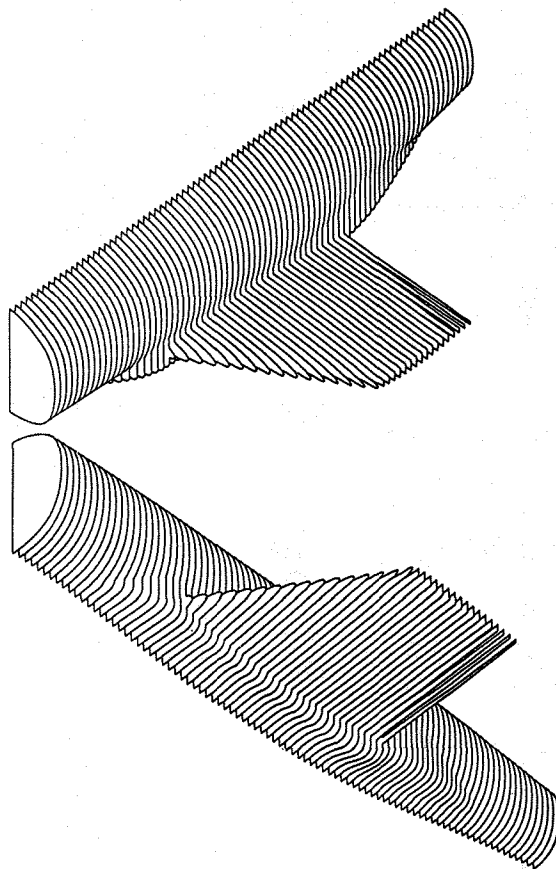


Fig.25-26. Civil aircraft with the new fairing, views from above and from below.

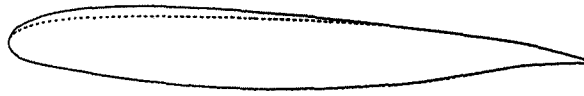


Fig.27. Wing - fairing root section, $\eta = .12$.
 ---- old fairing, — new fairing.

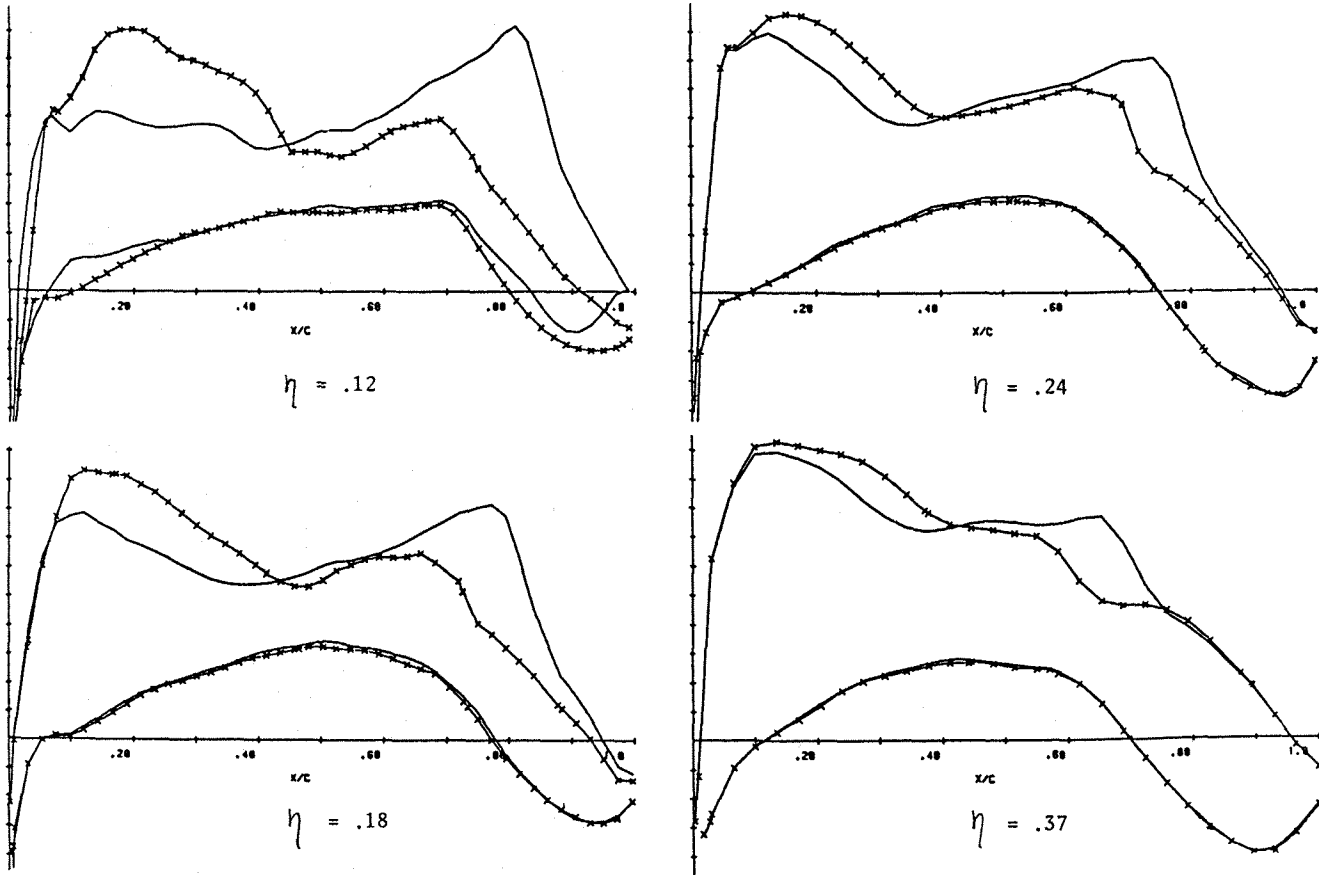


Fig.28. C_p distribution at several wing - fairing inboard sections, with old and new fairing.

$M = .8, \alpha = 1.5^\circ$.

— with the old fairing,
 -x-x-x- with the new fairing.